

A Leptonic Interpretation of the UHE Gamma-ray Emission from V4641 Sgr

SU-YU WAN,^{1,2} JIE-SHUANG WANG,³ AND RUO-YU LIU^{1,2,4}

¹*School of Astronomy and Space Science, Nanjing University, Nanjing 210023, China*

²*Key laboratory of Modern Astronomy and Astrophysics(Nanjing University),Ministry of Education,Nanjing 210023, People's Republic of China*

³*Max Planck Institute for Plasma Physics, Boltzmannstraße 2, D-85748 Garching, Germany*

⁴*Tianfu Cosmic Ray Research Center, Chengdu 610000, Sichuan, China*

ABSTRACT

Recently, the microquasar V4641 Sgr and its surrounding is detected at TeV-PeV gamma-ray band. Interestingly, the spectrum follows a power-law function continuing up to 0.8 PeV as reported by LHAASO, and the morphology of the emission appears a puzzling elongated structure. In this work, we propose that the elongated UHE emission from V4641 Sgr could originate from the inverse Compton radiation of electrons with a very hard spectrum, which may result from shear acceleration mechanism in the jets driven by V4641 Sgr. We also calculate the corresponding X-ray synchrotron emission from the same electron population, predicting the potential range of non-thermal X-ray flux of the source. The recent observation by XRISM toward the central part of the UHE source could pose a constraint on the model parameters. In the future, a full coverage of the source by sensitive X-ray instrument and high-resolution TeV-PeV gamma-ray instrument may provide a critical test of the model.

Keywords: Binary stars (154) — Plasma jets (1263) — Non-thermal radiation sources (1119)

1. INTRODUCTION

Microquasars are a subclass of X-ray binary systems (V. Bosch-Ramon & D. Khangulyan 2009), composed of an accreting compact object and a donor companion star. In the process of mass transfer, structures like relativistic jets could be formed. Microquasars has been found in our own Milky Way, so their jets could be spatially resolved by TeV gamma-ray instrument with angular resolution of $\sim 0.1^\circ$. They may serve as natural laboratories for studying particle acceleration in relativistic jets. Recently, five microquasars have been detected at UHE gamma-ray band by the Large High Altitude Air Shower Observatory (LHAASO), High Altitude Water Cherenkov Observatory (HAWC), and High Energy Stereoscopic System (H.E.S.S.). Among these microquasars, V4641 Sgr, a very active low-mass X-ray binary located at 6.2 kpc away from Earth (R. K. MacDonald et al. 2014; P. Gandhi et al. 2019), stands out for the gamma-ray spectrum which continues up to 0.8 PeV following a power-law distribution of slope -2.67 above 40 TeV (LHAASO Collaboration 2024). Such

high-energy photons indicates the presence of efficient particle acceleration in this system. The morphology of the UHE gamma-ray source shows an elongated morphology (LHAASO Collaboration 2024; R. Alfaro et al. 2024), and the physical size along the extension direction reaches ~ 100 pc. The morphological analysis shows that the emission may be also fitted by two “lobes”. R. Alfaro et al. (2024) suggested that the emission of V4641 Sgr is due to hadronic radiation of protons accelerated by jet termination shocks. The source is also suggested to be produced by escaping protons (Y. Ohira 2024; A. Neronov et al. 2025), where the elongated morphology could be ascribed to the topology of the local Galactic magnetic field (A. Neronov et al. 2025).

While these studies all proposed hadronic origin of the UHE gamma-ray emission, the leptonic scenario, in which the UHE photons are generated by inverse Compton (IC) radiation of high-energy electrons, has not been investigated in depth. Indeed, the hadronic scenario has a few advantages than the leptonic scenario in explaining the spectrum and the large extension of the source. First, protons do not suffer strong radiative cooling, so it would be easier for protons to be accelerated to PeV level and diffuse over a large distance. Second, the gamma-ray spectrum of hadronic radiation

approximately follow that of protons, whereas the inverse Compton (IC) radiation of electrons at UHE band will suffer the Klein-Nishina (KN) effect and generally a softening is expected. However, these issues of the leptonic scenario are addressable given specific conditions.

In this study, we aim to investigate that whether the UHE emission associated with V4641 Sgr can be explained under the leptonic scenario. We envisage the following picture: the frequent outbursts of V4641 Sgr has formed a pair of quasi-continuous jets. At $b = -4.8^\circ$ and 6.2 kpc from Earth, the microquasar is located at about 500 pc above the Galactic plane, so the density of the ambient medium is lower than the typical ISM density. Consequently, instead of being terminated at relatively small distance, the two mildly-relativistic jets have propagated to ~ 100 pc scale away from the central black hole. A velocity shear across the jet or spine-layer structure may form because of the interaction with the ambient medium (J.-S. Wang et al. 2023). A ‘distributed’ acceleration of electrons along the jet may then occur via the shear acceleration (SHA) mechanism (E. Berezhko & G. Krymskii 1981; J. Earl et al. 1988; F. M. Rieger & P. Duffy 2006; R.-Y. Liu et al. 2017; G. Webb et al. 2018; G. M. Webb et al. 2019; F. M. Rieger 2019; J.-S. Wang et al. 2024), which help explain the large extension of the source. Such a mechanism has been suggested to explain the kpc-scale TeV jet seen in Centaurus A by H.E.S.S. (H. E. S. S. Collaboration et al. 2020) and extended X-ray emissions in kpc-Mpc scale jets launched from some radio galaxies (R.-Y. Liu et al. 2017; J.-S. Wang et al. 2021; J.-C. He et al. 2023). A hard particle spectrum is also expected in the SHA mechanism, which may overcome the KN effect and produce a hard spectrum with a power-law form approximately up to PeV energy (R.-Y. Liu & X.-Y. Wang 2021).

The rest of the paper is organized as follows: in Section 2, we introduce our method and the model setup; in Section 3, we show our fitting results to the gamma-ray data and constraints from X-ray observations; we discuss our model in Section 4 and give conclusions in Section 5.

2. MODEL AND METHODS

2.1. The jet model and electron spectra

Considering the interactions between a jet and its surrounding medium, deceleration of the jet may occur in the boundary region, while the central velocity remains nearly unchanged. Hence a velocity gradient along the transverse direction of the jet axis may form. Such jets with velocity shear have been reported in some high-resolution radio observations (H. Nagai et al. 2014; D. C. Gabuzda 2014; R. Laing & A. Bridle 2014). It has been

suggested that particles can be scattered off magnetic turbulence frozen in different velocity layers throughout the jet, gaining energies after sufficient times of scatterings (F. M. Rieger & P. Duffy 2006), which is a kind of second-order Fermi particle acceleration mechanism. The acceleration rate is related to the shear velocity profile. In this work we assume that the jet is composed of a central spine with constant speed β_0 (in unit of the speed of light c) and a velocity-shear boundary, and for simplicity a linear profile is adopted as

$$\beta(r) = \begin{cases} \beta_0 & 0 \leq r < (1 - \eta) R_{\text{jet}}, \\ \frac{\beta_0}{\eta} \left(1 - \frac{r}{R_{\text{jet}}}\right) & (1 - \eta) R_{\text{jet}} \leq r \leq R_{\text{jet}}. \end{cases} \quad (1)$$

Here η is a dimensionless parameter, indicating the ratio between the size of the velocity-shear boundary (R_{SHA}) and the radius of the jet (R_{jet}). With the assumed velocity profile, velocity gradients ($\partial\beta/\partial r$) in the two flow regions can also be readily calculated.

SHA generally has a higher acceleration rate when accelerating higher-energy particles. Therefore, at low energies it requires ‘seed particles’ pre-accelerated by other mechanism, since otherwise the overall acceleration would become inefficient. It has been demonstrated that (R.-Y. Liu et al. 2017) the stochastic acceleration (STA) accompanies with the SHA, and can naturally serve as pre-acceleration process although itself is not an efficient mechanism in weakly magnetized jets. Both STA and SHA can be regarded as ‘diffusion’ processes in the momentum phase space of particles, and acceleration process can be described with the Fokker-Planck-type equation (F. M. Rieger et al. 2007; R.-Y. Liu et al. 2017). For simplicity, we assume the diffusion is isotropic. Here the equation is written in the energy form, which reflects the energy distribution of accelerated particles more directly:

$$\begin{aligned} \frac{\partial n(\gamma, t)}{\partial t} = & \frac{1}{2} \frac{\partial}{\partial \gamma} \left[\left\langle \frac{\Delta \gamma^2}{\Delta t} \right\rangle \frac{\partial n(\gamma, t)}{\partial \gamma} \right] \\ & - \frac{\partial}{\partial \gamma} \left[\left(\left\langle \frac{\Delta \gamma}{\Delta t} \right\rangle - \frac{1}{2} \frac{\partial}{\partial \gamma} \left\langle \frac{\Delta \gamma^2}{\Delta t} \right\rangle + \langle \dot{\gamma}_c \rangle \right) n(\gamma, t) \right] \\ & - \frac{n(\gamma, t)}{t_{\text{esc}}} + Q(\gamma, t). \end{aligned} \quad (2)$$

The left-side term describes the time-dependent evolution of particle distribution $n(\gamma, t)$ in the phase space of energy.

To solve Eq. (2) for both STA and SHA scheme, it is necessary to figure out corresponding Fokker-Planck coefficients $\langle \Delta \gamma / \Delta t \rangle$ and $\langle \Delta \gamma^2 / \Delta t \rangle$, which can be obtained through a series of microscopic treatments and approximations (J. Jokipii & G. Morfill 1990; F. M. Rieger & P. Duffy 2006; R.-Y. Liu et al. 2017). In the

following calculations, the accelerated particles will be set as electrons with rest mass m_e . The Fokker-Planck relation (F. M. Rieger & P. Duffy 2006) connecting the momentum diffusion coefficient and the momentum variation coefficient can be rewritten in the energy space as:

$$\left\langle \frac{\Delta\gamma}{\Delta t} \right\rangle = \frac{1}{2\gamma^2} \frac{\partial}{\partial\gamma} \left[\gamma^2 \left\langle \frac{\Delta\gamma^2}{\Delta t} \right\rangle \right]. \quad (3)$$

For STA, denoting the Alfvén velocity of the plasma by v_A , the diffusion coefficient in the momentum space is proportional to $v_A^2 p^2 / \kappa$ according to the quasi-linear theory (R. Schlickeiser et al. 2002). Here $\kappa = c^2 \tau_{sc} / 3$, representing the spatial diffusion coefficient of particles; And τ_{sc} is the mean scattering timescale, denoting the time between two scattering events:

$$\tau_{sc} = \frac{r_L^{2-q}}{c\xi\Lambda_{\max}^{1-q}}. \quad (4)$$

With the expression in Eq. (4), the energy diffusion coefficient takes the form below if Alfvén wave is regarded as the only type of Magnetohydrodynamic (MHD) wave that scatter off particles:

$$\left\langle \frac{\Delta\gamma^2}{\Delta t} \right\rangle_{STA} = \frac{\xi\Gamma_A^4 \beta_A^2 c}{r_L^{2-q} \Lambda_{\max}^{q-1}} \gamma^2 = A_{STA} \gamma^q, \quad (5)$$

$$A_{STA} = \frac{\xi\Gamma_A^4 \beta_A^2 c}{\Lambda_{\max}^{q-1}} \left(\frac{m_e c^2}{eB_0} \right)^{q-2}. \quad (6)$$

where β_A denotes the dimensionless Alfvén speed of the jet and Γ_A represents its bulk Lorentz factor; $\xi = (\delta B / B_0)^2$, reflecting the strength of magnetic turbulence. r_L is the Lamor radius of an electron whose energy is $\gamma m_e c^2$ and Λ_{\max} is the longest wavelength of the MHD wave modes. The index q is related to the power-law turbulence spectrum ($W(k) \propto k^{-q}$) of MHD waves (P. Mertsch 2011), whose typical values include 5/3 (Kolmogorov-type), 3/2 (Kraichnan-type), 1 (Bohm-type) and 2 ('hard-sphere' limit). With Fokker-Planck relation, the energy variation coefficient can be calculated as:

$$\left\langle \frac{\Delta\gamma}{\Delta t} \right\rangle_{STA} = \frac{(2+q) A_{STA}}{2} \gamma^{q-1}. \quad (7)$$

Then the acceleration timescale can be estimated using $t_{acc,STA} = \gamma / \langle \Delta\gamma / \Delta t \rangle_{STA}$, and we get:

$$t_{acc,STA} = \frac{2}{(2+q) A_{STA}} \gamma^{2-q}. \quad (8)$$

For the SHA, the Fokker-Planck coefficients in the energy space are written in following forms (F. M. Rieger

& P. Duffy 2006; R.-Y. Liu et al. 2017; F. M. Rieger & P. Duffy 2019; J.-S. Wang et al. 2021):

$$\left\langle \frac{\Delta\gamma^2}{\Delta t} \right\rangle_{SHA} = \frac{2}{15} \Gamma_j^4 \left(\frac{\partial\beta_j}{\partial r} \right)^2 c^2 \tau_{sc} \gamma^2, \quad (9)$$

$$\left\langle \frac{\Delta\gamma}{\Delta t} \right\rangle_{SHA} = \frac{6-q}{15} \Gamma_j^4 \left(\frac{\partial\beta_j}{\partial r} \right)^2 c^2 \tau_{sc} \gamma, \quad (10)$$

β_j represents the flow speed in the velocity-shear layer j , and Γ_j is the corresponding bulk Lorentz factor.

The acceleration timescale for SHA can be obtained with the relation $t_{acc,SHA} = \gamma / \langle \Delta\gamma / \Delta t \rangle_{SHA}$. Just as what has been discussed in the previous section, SHA can only happen in regions where velocity gradients exist. This mechanism will not work in the central spine region of the jet. So we average both $\langle \Delta\gamma^2 / \Delta t \rangle_{SHA}$ and $\langle \Delta\gamma / \Delta t \rangle_{SHA}$ over the transverse radius of the jet, in order to simply the treatment of the particle acceleration within the entire jet (so that we do not need to introduce an additional space dimension in the Fokker-Planck equation). It results in

$$\overline{\left\langle \frac{\Delta\gamma^2}{\Delta t} \right\rangle}_{SHA} = \frac{\int_0^{R_{jet}} 2\pi r \langle \frac{\Delta\gamma^2}{\Delta t} \rangle_{SHA} dr}{\pi R_{jet}^2}, \quad (11)$$

and

$$\overline{\left\langle \frac{\Delta\gamma}{\Delta t} \right\rangle}_{SHA} = \frac{\int_0^{R_{jet}} 2\pi r \langle \frac{\Delta\gamma}{\Delta t} \rangle_{SHA} dr}{\pi R_{jet}^2}. \quad (12)$$

Substituting Eq. (1), (9) into Eq. (11) and Eq. (1), Eq. (10) into Eq. (12), we can get modified Fokker-Planck coefficients, written as:

$$\overline{\left\langle \frac{\Delta\gamma^2}{\Delta t} \right\rangle}_{SHA} = \frac{2}{15} \overline{\Gamma_j^4} \left(\frac{\beta_0}{\eta R_{jet}} \right)^2 c^2 \tau_{sc} \gamma^2 = \bar{A}_{SHA} \gamma^{4-q}, \quad (13)$$

$$\overline{\left\langle \frac{\Delta\gamma}{\Delta t} \right\rangle}_{SHA} = \frac{6-q}{15} \overline{\Gamma_j^4} \left(\frac{\beta_0}{\eta R_{jet}} \right)^2 c^2 \tau_{sc} \gamma = \frac{6-q}{2} \bar{A}_{SHA} \gamma^{3-q}, \quad (14)$$

with

$$\overline{\Gamma_j^4} = \frac{\eta}{2\beta_0} \left[\ln \left(\frac{1+\beta_0}{1-\beta_0} \right) + \frac{2\beta_0}{1-\beta_0^2} \right] - \frac{\eta^2}{1-\beta_0^2}. \quad (15)$$

and

$$\bar{A}_{SHA} = \frac{2}{15} \overline{\Gamma_j^4} \left(\frac{\beta_0}{\eta R_{jet}} \right)^2 \xi^{-1} \Lambda_{\max}^{q-1} \left(\frac{m_e}{eB_0} \right)^{2-q} c^{5-2q}. \quad (16)$$

Those averaged coefficients will be used in further calculations.

Particle acceleration may be hindered by energy loss and escape. We assume the energy loss are dominated

by $\dot{\gamma}_c \propto -\gamma^2$ type radiative cooling process such as synchrotron radiation and IC radiation in the Thomson regime:

$$\langle \dot{\gamma}_c \rangle = -\frac{\sigma_T B_0^2 \gamma^2}{6\pi m_e c} (1 + X) = -A_c \gamma^2, \quad (17)$$

where σ_T is the Thomson cross section of electrons, $X = u_{\text{rad}}/u_B$ with $u_B = B_0^2/(8\pi)$ and u_{rad} the energy density of the target photon field. Above a few tens of TeV the IC scattering is dominated by the Cosmic Microwave Background (CMB) (D. Khangulyan et al. 2014), and hence the value of u_{rad} is set as 4.2×10^{-13} erg/cm³, corresponding to the local energy density of CMB background. The timescale for the diffusive escape of electrons from the jet can be given by

$$t_{\text{esc}} = \frac{R_{\text{jet}}^2}{2\kappa} = A_{\text{esc}} \gamma^{q-2}, \quad (18)$$

$$A_{\text{esc}} = \frac{3R_{\text{jet}}^2 \xi \Lambda_{\text{max}}^{1-q}}{2c} \left(\frac{eB_0}{m_e c^2} \right)^{2-q}. \quad (19)$$

Note that Eq. (4) is valid only when the resonant scattering of wave-particle interaction is applied. In this condition, the scattering of a particle is dominated by the wave whose wavelength is comparable to the Larmor radius of the particles ($r_L \sim 1/k$, or the first-order resonance for particles of small rigidity) (C. Demidem et al. 2020; R. M. Kulsrud 2020). As the energy of particle exceeds $\gamma_{\text{rsn}} \equiv eB_0 \Lambda_{\text{max}} m_e^{-1} c^{-2}$, its Larmor radius exceed the longest wavelength Λ_{max} . The wave-particle scattering timescale would then deviate from Eq. (4), and high-order resonance needs to be considered. It leads to a modification of the expression of the scattering timescale, which can be given by $\tau_{\text{sc}} = r_L^2 (c\xi \Lambda_{\text{max}})^{-1}$ (see Appendix A for the derivation). The coefficients involving τ_{sc} (from Eq. (4) to Eq. (19)) should also be modified correspondingly.

With all coefficients obtained, we may set to solve the Fokker-Planck equation. Although the exact age of the black hole - jet system in V4641 Sgr remains unknown, considering its B9III companion star (R. K. MacDonald et al. 2014), a quasi-continuous jet may exist for a sufficient long time, and thus we consider a quasi-steady state by setting $\partial n(\gamma, t)/\partial t = 0$. Substituting Eqs. (13)-(18) into Eq. (2), the equation for SHA scheme is rewritten as:

$$\frac{\partial^2 n}{\partial \gamma^2} + C_1(\gamma) \frac{\partial n}{\partial \gamma} + C_2(\gamma) n + 2Q \bar{A}_{\text{SHA}}^{-1} \gamma^{q-4} = 0, \quad (20)$$

where

$$C_1(\gamma) = (2 - q) \gamma^{-1} + 2A_c \bar{A}_{\text{SHA}}^{-1} \gamma^{q-2}, \quad (21)$$

and

$$C_2(\gamma) = 4A_c \bar{A}_{\text{SHA}}^{-1} \gamma^{q-3} - (2A_{\text{esc}}^{-1} \bar{A}_{\text{SHA}}^{-1} - 2q + 6) \gamma^{-2}. \quad (22)$$

The injection term Q is usually considered as a Dirac- δ function, such as $Q = \delta(\gamma - \gamma_{\text{eq}})$. Particles are usually injected to the acceleration process from the thermal pool (i.e., $\gamma_{\text{eq}} \gtrsim 1$), where STA dominates. SHA starts to take over the STA when $\langle \Delta\gamma/\Delta t \rangle_{\text{STA}} = \langle \Delta\gamma/\Delta t \rangle_{\text{SHA}}$, or at $\gamma = \gamma_{\text{eq}}$ with

$$\gamma_{\text{eq}} = \left[\frac{(2+q) A_{\text{STA}}}{(6-q) \bar{A}_{\text{SHA}}} \right]^{\left(\frac{1}{4-2q} \right)}, \quad (q \neq 2). \quad (23)$$

Therefore, we simply consider $Q = 0$ in Eq. (20) since we focus on the acceleration of TeV-PeV particles.

At $\gamma < \gamma_{\text{eq}}$, the STA dominates and the accelerated spectrum can be given by (R.-Y. Liu et al. 2017):

$$N_1(\gamma) = -\frac{2C\gamma}{(1+q) A_{\text{STA}} \gamma^q} \propto \gamma^{1-q}, \quad (24)$$

which is a single power-law spectrum.

J.-S. Wang et al. (2021) analytically solve Eq. (20) with $Q = 0$ for $1 < q \leq 2$: Substituting trial solutions with the form of $n(\gamma) \propto \gamma^s j(\gamma)$ and introducing a new variable $z = (6-q)/(1-q)(\gamma/\gamma_{\text{max}})^{q-1}$ (γ_{max} equals to the γ value where $t_{\text{acc,SHA}} = t_c$), $j(z)$ can be expressed in a Kummer-form differential equation, whose general solutions are combinations of confluent hyper-geometric functions, denoted by ${}_1F_1$ (M. Abramowitz & I. A. Stegun 1948). The final solution for $n(\gamma)$ is:

$$N_2(\gamma) = K_1 \gamma^{s+1} {}_1F_1(a_+, b_+; z) + K_2 \gamma^{s-1} {}_1F_1(a_-, b_-; z), \quad (25)$$

where $a_{\pm} = (2 + s_{\pm})/(q-1)$, $b_{\pm} = 2s_{\pm}/(q-1)$, $s_{\pm} = (q-1)/2 \pm \sqrt{(5-q)^2/4 + w}$, $w = (6-q)t_{\text{acc,SHA}}/t_{\text{esc}}$, and both K_1 and K_2 are normalization factors. In our spectral model, $w = 10\eta^2/(\beta_0^2 \Gamma_j^4)$. Eq. (25) is valid to describe the accelerated electron spectrum for $\gamma_{\text{eq}} < \gamma < \gamma_{\text{rsn}}$ and the low-order resonance is satisfied ($\gamma < \gamma_{\text{rsn}}$). Note that s_+ is always larger than 0, so we have $K_1 = 0$ based on the boundary condition $N_2(\gamma \rightarrow \infty) \rightarrow 0$.

At $\gamma > \gamma_{\text{rsn}}$, the particle spectrum is subject to change at $\gamma > \gamma_{\text{rsn}}$ due to the modified scattering rate. The solution for the Fokker-Planck equation of SHA at this energy range is found to be in a power-law form:

$$N_3(\gamma) = D_1 \gamma^{p+} + D_2 \gamma^{p-}, \quad (26)$$

where $p_{\pm} = -1/2 \pm \sqrt{25/4 + w}$. The complete derivation is shown in Appendix B. Similarly, $p_+ > 0$ is always established so we have $D_1 = 0$ based on the boundary condition $N_3(\gamma \rightarrow \infty) \rightarrow 0$.

Combing Eq. (24) Eq. (25) and Eq. (26), the model for electron spectrum considering both stochastic and shear acceleration can be summarized as the piecewise function shown below:

$$N(\gamma) = \begin{cases} K_0\gamma^{1-q} & \gamma < \gamma_{\text{eq}}, \\ K_2\gamma^{s-1}F_1(a_-, b_-; z) & \gamma_{\text{eq}} \leq \gamma < \gamma_{\text{rsn}}, \\ D_2\gamma^{p-} & \gamma_{\text{rsn}} \leq \gamma. \end{cases} \quad (27)$$

To maintain the continuity of the spectrum, we have $N_1(\gamma_{\text{eq}}) = N_2(\gamma_{\text{eq}})$ and $N_2(\gamma_{\text{rsn}}) = N_3(\gamma_{\text{rsn}})$ so that the normalization factors could be obtained. Given the boundary condition, the normalization coefficients are replaced by a single free parameter indicating the total number of accelerated electrons: $N_{\text{tot}} = \int_{\gamma_{\text{min}}}^{+\infty} N(\gamma)d\gamma$, which efficiently simplifies the parameter space. Here $\gamma_{\text{min}} \sim 2$, corresponding to MeV electrons.

2.2. Parameter constraints

The cooling term and the escaping term in the Fokker-Planck equation serve as natural constraints on the parameters, for the spectrum would be quite steep if the two terms become dominated. In order to preliminary narrow down the parameter space, the influences of cooling and diffusive escape should be discussed.

By equating the acceleration rate Eq. (14) and the cooling rate Eq. (17), the maximum energy γ_{max} is achieved when $t_{\text{acc,SHA}} = t_c$, written as:

$$\gamma_{\text{max}} = \left[\frac{(6-q)\bar{A}_{\text{SHA}}}{2A_c} \right]^{\frac{1}{q-1}}. \quad (28)$$

If $\gamma > \gamma_{\text{max}}$, the spectrum would present a cutoff due to the effects of cooling. As to the diffusive escape, it becomes more efficient at higher energy as long as $1 < q \leq 2$. For the SHA, the dependence of the acceleration timescale and the escape timescale on particle energy is the same. If the escape timescale is shorter than the acceleration timescale, the accelerated spectrum would be significantly softened. In order to maintain a hard electron spectrum, the escape timescale should not be much shorter than that for the SHA, i.e. $t_{\text{acc,SHA}} \lesssim t_{\text{esc}}$

$$\eta \lesssim [\beta_0 \ln \left(\frac{1+\beta_0}{1-\beta_0} \right) + \frac{2\beta_0^2}{1-\beta_0^2}] \left(\frac{20}{6-q} + \frac{2\beta_0^2}{1-\beta_0^2} \right)^{-1}. \quad (29)$$

Eq. (29) tells that the velocity-shear region should be small enough to achieve a sufficiently high acceleration efficiency.

Concerning that when $q = 5/3$, the SA spectrum becomes too hard to fit to the observed spectrum, we speculate that in this case the spectrum above a TeV would not be dominated by SA. This requires that $\gamma_{\text{eq}}m_e c^2$

should not significantly exceed 1 TeV to ensure the domination of SHA above 1 TeV:

$$A_{\text{STA}} \lesssim \frac{(6-q)\bar{A}_{\text{SHA}}}{(2+q)}\gamma^{(4-2q)}, \quad (30)$$

for $\gamma \sim 1\text{TeV}/(m_e c^2)$. Once n_p becomes too small, Eq. (30) could no longer be satisfied.

Aside from these constraints, the observations of V4641 Sgr pose additional restrictions on the parameters, which are listed as follows:

1. **The maximum luminosity:** According to historical X-ray observations, the most luminous flare from the microquasar in 1999 reached a luminosity of $\sim (3-4) \times 10^{39}$ erg/s over 1-10 keV (M. Revnivtsev et al. 2002), which exceeds the Eddington luminosity of a $10M_{\text{sun}}$ black hole. As a conservative estimate, the long-term average kinetic luminosity of the quasi-continuous jet, defined as the total kinetic energy of particles flowing through the jet's cross section per second, should not significantly exceed the Eddington luminosity:

$$L_{\text{kin}} = \pi(1-\eta)^2 R_{\text{jet}}^2 n_p \Gamma(\Gamma-1) m_p c^2 (\beta_0 c) \leq L_{\text{Edd}}, \quad (31)$$

where $\Gamma = 1/\sqrt{1-\beta_0^2}$ is the bulk Lorentz factor of the jet's spine (here we neglect the kinetic luminosity of the velocity-shear region); n_p represents the number density of protons in the jet. Assuming $L_{\text{Edd}} = 1.3 \times 10^{39}$ erg/s, Eq. (31) gives the approximation for the maximum protons' number density of the jet:

$$n_p \lesssim 4 \times 10^{-8} [\Gamma(\Gamma-1)]^{-1} \beta_0^{-1} (1-\eta)^{-2} \left(\frac{R_{\text{jet}}}{5 \text{ pc}} \right)^{-2} \text{ cm}^{-3}. \quad (32)$$

2. **Confinement of particles:** During acceleration processes, the electrons should be confined in the acceleration region. That is to say, their gyro-radius r_L should be smaller than the characteristic length of the accelerator R_{jet} , which is roughly equivalent to the Hillas criterion with $\beta_0 \lesssim 1$ (A. M. Hillas 1984). It therefore provides a constraint on the maximum particle energy by

$$\gamma_{\text{Hillas}} = \frac{eB_0 R_{\text{jet}}}{m_e c^2}. \quad (33)$$

If $\gamma > \gamma_{\text{Hillas}}$, the electrons will quickly escape the jet, leading to a cutoff in the spectrum around γ_{Hillas} . Moreover, if the mean free path (MFPs, λ) of the electrons is comparable to or longer than the radius of the jet ($\lambda = c\tau_{\text{sc}} < R_{\text{jet}}$), particles can escape the jet without being scattered and cannot be

described with the Fokker-Planck equation, leading to a cutoff in the accelerated spectrum around the energy γ_{MFP} which is defined by $c\tau_{\text{sc}} = R_{\text{jet}}$ or

$$\gamma_{\text{MFP}} = \frac{eB_0}{m_e c^2} (\xi \Lambda_{\text{max}}^{1-q} R_{\text{jet}})^{\frac{1}{2-q}}, \quad (34)$$

where $\Lambda_{\text{max}} = \eta R_{\text{jet}}$ is employed in the calculation, i.e., the longest wavelength of turbulence is equal to the transverse size of the velocity-shear region. This is a conservative assumption because the Λ_{max} can be in principle comparable to the entire size of the jet and the constraint on the maximum particle energy may be relaxed. This constraint can be also expressed by $\xi^{-1}(r_L/\Lambda_{\text{max}})^{1-q} r_L < R_{\text{jet}}$. The constraint on the maximum energy is generally stronger than the Hillas criterion for relativistic flow ($\beta_0 \lesssim 1$), unless in the Bohm limit ($\xi = 1$ and $q = 1$).

With those constraints, we can roughly figure out the range of some parameters. For a leptonic interpretation of the LHAASO observation, electrons must be accelerated to at least 0.8 PeV. Given the aboved equations being satisfied, constraints on the magnetic field and η could be obtained, which are shown in Figure 1. According to calculations, B_0 could vary within a wide range, from less than 0.1 μG to around 100 μG when $R_{\text{jet}} = 5$ pc; Eq. (32) indicates that the jet can not be ultra-relativistic, or the upper limit of the density might be smaller than its lower limit. This leads to another conclusion that the size of the velocity-shear region is limited to a relatively small range, which is consistent with common astrophysical conditions.

3. RESULTS

3.1. Fitting to the gamma-ray data

We then fit the observational data with derived spectral model, taking into account constraints obtained in section 2.2. Our spectrum model contains four main free parameters: B_0 , η , β_0 , and N_{tot} . For other parameters, we set ξ to 1, denoting that $\delta B_0 \sim B_0$. A smaller ξ would lead to higher SHA rate. q is set to 5/3, corresponding to the Kolmogorov-type turbulence. Λ_{max} is given by $\Lambda_{\text{max}} = \eta R_{\text{jet}}$. In our model, shear-accelerated electrons are responsible for observed TeV - PeV photons via IC scattering. `naima`, a python package which can compute the non-thermal radiation from given electron populations (V. Zabalza 2015) is used to calculate the IC emission produced by the modeled electron distribution. Implements precise analytical solutions for the IC scattering of black-body seed photons (D. Khangulyan et al. 2014), which is computationally cheap and can achieve high precision under both the Thomson and KN

limits. Here three types of seed photon field are selected to calculate the radiation, including CMB, Far-Infrared (FIR) and Near-Infrared (NIR).

The inclination angle of the jet is unclear. However, results from the ellipsoidal orbital fittings with the ELC code (R. K. MacDonald et al. 2014) show that the inclination angle i of the source, which is defined as the angle between the direction perpendicular to the binary orbital plane and the observer's line of sight, is $72.3 \pm 4.1^\circ$. In a standard binary system, the accretion disk is parallel with the orbital plane due to the conservation of momentum and the jet is nearly perpendicular to the disk (R. D. Blandford & R. L. Znajek 1977), so we set the jet angle as 72.3° when computing the relativistic beaming effect to match the recent UHE observations.

For a source distance of $d = 6.2$ kpc, the attenuation of high-energy gamma-ray photons need be taken into consideration, because the typical attenuation length of PeV photons absorbed by CMB is $\lesssim 8$ kpc (P. S. Coppi & F. A. Aharonian 1997; C. D. Dermer & G. Menon 2009), comparable to the source distance. So we compute the optical depth $\tau_{\gamma\gamma}$, based on which we correct the results of `naima` to obtain the observed flux.

MCMC is a powerful algorithm to find the best-fit parameters for a model basing on Bayesian methods. We use the Python package `emcee` to carry out the fittings. The observational data mainly comes from two experiments: LHAASO (LHAASO Collaboration 2024) and HAWC (R. Alfaro et al. 2024). To explore the parameter space more efficiently, all parameters, except η and β_0 , are redefined in their logarithmic forms. The auto-correlation time is calculated to ensure convergence of the results, and constraints in section 2.2 are used to define the prior function. Data collected from H.E.S.S. observatory, ranging from 1 to 40 TeV is extracted from A. Neronov et al. (2025) to further constrain the model. All parameters and their best-fit values are shown in Table 1. The UHE spectrum can be well reproduced with the IC radiation of accelerated electrons under all R_{jet} considered, as shown in Figure 2.

Within the framework of SHA, the obtained magnetic field depends on the assumed radius of the jet. A larger B_0 is required for a smaller R_{jet} , due to the requirement of confinement as discussed in section 2.2. On the other hand, the velocity of the jet spine keeps more or less the same ($\sim 0.6c - 0.7c$) for different R_{jet} . Based on these parameters, the baryon density of the jet n_p may range from $2.5 \times 10^{-11} \text{ cm}^{-3}$ to $2.6 \times 10^{-7} \text{ cm}^{-3}$ for $R_{\text{jet}} = 5$ pc (the largest R_{jet} employed), and from $3.6 \times 10^{-9} \text{ cm}^{-3}$ to $3.0 \times 10^{-5} \text{ cm}^{-3}$ for $R_{\text{jet}} = 0.5$ pc (the smallest R_{jet} employed), according to the constraints from Eqs. (30) and (31). Note that n_p has little impact on the obtained

electron spectrum as long as it is within the reasonable range. The wide available range of n_p shows that the model parameters are self-consistent.

In section 2.1, we have obtained all timescales from Eq. (4), (7), (14), (17) and Eq. (18). With the best-fit parameters for the model, all timescales are shown in Figure 3. As we expected, STA dominates the acceleration at low energies ($\gamma < \gamma_{\text{eq}}$), providing ‘seed particles’, and SHA becomes more important at $\gamma > \gamma_{\text{eq}}$. Acceleration of particles around $\gamma \sim \gamma_{\text{eq}}$ takes the longest time, which is about a few times 10^{10} s for all four cases. It implies that the system must exist for at least a few thousand years, or otherwise we cannot apply the quasi-steady state solution. For such a duration of time, the jet is able propagate to ~ 100 pc away from the BH with a mildly-relativistic velocity, although the speed of the jet head could have been decelerated to non-relativistic. We also find that $t_{\text{acc,SHA}} \lesssim t_{\text{esc}}$ in all four cases. This is not a coincidence. From Fig. 2 we see that the gamma-ray photon index from 1 TeV to a few times 100 TeV (before the softening/cutoff occurs) is approximately $\lesssim -1.5$, so we need approximately $N(\gamma) \propto \gamma^{-2}$ to reproduce the observed spectrum, or $s_- = (q-1)/2 - \sqrt{(5-q)^2/4 + w} = -2$. This gives $t_{\text{acc,SHA}}/t_{\text{esc}} = w/(6-q) = 4(q-1)/(6-q)$. For $1 < q \leq 2$, we generally have $t_{\text{acc,SHA}}/t_{\text{esc}} \lesssim 1$. $t_{\text{acc,SHA}}/t_{\text{esc}} \lesssim 1$ implies a relatively efficient escape of accelerated electrons. These electrons may produce a halo-like UHE structure in the surrounding ISM via IC radiation, making the source more extended than the transverse size of the jet.

3.2. X-ray synchrotron emission

In the emission region, accelerated electrons will also generate synchrotron radiation when traversing the magnetic field. For TeV - PeV electrons in a magnetic field at the microgauss level, the radiation should peak at the X-ray band. Within the SHA scenario, we can predict the X-ray synchrotron emission from the electrons which are responsible for the detected UHE emission. The `naima` package is also used to calculate the synchrotron emission, based on the emissivity function in random magnetic fields (F. Aharonian et al. 2010). The results are shown in Figure 4. With the best-fit parameters, the unabsorbed total X-ray flux in 2 – 10 keV varies from 10^{-13} to 10^{-12} erg cm $^{-2}$ s $^{-1}$ depending on R_{jet} and B_0 . Since the UHE gamma-ray and the non-thermal X-ray emission have the same origin in the leptonic model, we would expect an elongated morphology of the X-ray emission as well.

Recent observation of XRISM has revealed an extended X-ray source around V4641 Sgr, which may

constrain the model. The observation focuses on the central part of the microquasar, and the spatial extension is much smaller than the UHE structure detected by HAWC and LHAASO. They argued that if the X-ray emission is of non-thermal origin, its original electron population should be different from that responsible for the gamma-ray emission. Therefore, the surface brightness of the XRISM source, which is around $S_X = (7 - 10) \times 10^{-15}$ erg s $^{-1}$ cm $^{-2}$ arcmin $^{-2}$ in 2-10 keV (H. Suzuki et al. 2025), setup an upper limit of the synchrotron emission of accelerated electrons predicted in our model. We calculate the 2 – 10 keV flux from the whole jet, and compare it with the X-ray flux upper limit set by XRISM observation $S_X \Omega$. Here, $\Omega \approx 2R_{\text{jet}} \times 100 \text{ pc}/d^2 = 307 (R_{\text{jet}}/5 \text{ pc}) \text{ arcmin}^2$ is the solid angle of the jet subtended in the sky, with 100 pc being the projected length of the jet and $d = 6.2$ kpc being the distance of the microquasar. The X-ray flux upper limit for different R_{jet} are shown in Figure 4. We see that for $R_{\text{jet}} = 5$ pc and 3 pc, the predicted X-ray flux from the model is lower than the upper limit. When R_{jet} decreases to 1 pc, the predicted X-ray flux overshoots the upper limit even considering the lower bound of the parameter uncertainties. So we may conclude that $R_{\text{jet}} > 1$ pc is favored for this model. Note that since XRISM observations actually do not cover the full UHE emission region, the constraint may be relaxed if the future observations detect X-ray emission from UHE gamma-ray-emitting region outside its field of view.

4. DISCUSSION

4.1. Dependence on the turbulence spectrum q

Figures 2 and 4 present the results by assuming a Kolmogorov-type turbulence with $q = 5/3$. Actually, for other types of turbulence spectrum, the results will not change significantly unless for $q \rightarrow 1$. In Figure 5, we show the fitting to the gamma-ray spectrum and the predicted X-ray flux with $q = 3/2$ and $q = 2$, assuming $R_{\text{jet}} = 3$ pc. The main parameters do not vary much from those with $q = 5/3$, as shown in Table. 2, except for N_{tot} with $q = 2$. The reason is that the timescales of STA and SHA, as well as the escape timescale, all become energy-independent for $q = 2$. In this case, when the SHA dominates both low-energy and high-energy end, the spectrum is softened by the escape (see discussion in Section 3.1) and the accelerated spectrum becomes softer than γ^{-1} . The total electron number then significantly increase by integrating the spectrum down to $\gamma_{\text{min}} = 2$. Nevertheless, this corresponds to a total electron kinetic luminosity of $\sim 10^{36}$ erg/s, which is still reasonable. On the other hand, for $q \rightarrow 1$ the energy of the turbulence cascaded down to the gyro-scale of

electrons of relevant energies is much higher than those with larger q . As a consequence, the mean free path of electrons becomes smaller and hence the acceleration timescale of SHA will become longer (i.e., the SHA becomes less efficient). We find a higher jet velocity of $\beta_0 > 0.95$ is needed with $q = 1$. The relativistic effect becomes more important and the analytical solution derived in Section 2.1 may need modification.

4.2. Can STA work solely?

STA is also a ‘distributed’ acceleration, which may be helpful to explain the elongated morphology of UHE emission around V4641 Sgr in the leptonic scenario. In section 2.2, we discussed that the accelerated particle spectrum of STA is too hard to explain the measured spectrum of V4641 Sgr. However, with $q = 2$, the energy dependence of the acceleration timescale is the same with that of the escape timescale. In this case, when two timescales become comparable, the accelerated spectrum can be softened (similar to the SHA case) and the observed spectrum may be reproduced by pure STA with fine-tuning parameters. The main issue is the maximum particle energy achievable by STA. Indeed, strong turbulence and high Alfvén speed need be present in the environment for efficient STA, while observations of XRISM constrain the magnetic field strength to be lower than $\sim 1 \mu\text{G}$ in the jet. Therefore, a very low density would be needed to get a high Alfvén speed. From Figure 4, we see that there is still some room for a higher magnetic field in the cases of $R_{\text{jet}} = 5 \text{ pc}$ and 3 pc , which can be as high as $2 \mu\text{G}$ from the perspective of X-ray upper limit. On the other hand, a smaller Λ_{max} would lead to more efficient STA as long as the 1st-order resonance condition for 0.8 PeV electrons can be satisfied, i.e., $\gamma_{\text{rsn}} \equiv eB_0\Lambda_{\text{max}}m_e^{-1}c^{-2} \geq 0.8 \text{ PeV}/(m_e c^2)$ (otherwise, the STA becomes less efficient with high-order resonance). We take an optimistic setup for STA, i.e., $\xi = 1$, $B_0 = 2 \mu\text{G}$, and $\Lambda_{\text{max}} = 0.8 \text{ PeV}/(eB_0)$. Given these conditions, we require the acceleration timescale of STA to be shorter than the synchrotron cooling timescale for 0.8 PeV electrons, and we have

$$\Gamma_{\text{A}}^4 \beta_{\text{A}}^2 \geq A_c \Lambda_{\text{max}} \gamma (c\xi)^{-1} \quad (35)$$

for $\gamma = 0.8 \text{ PeV}/(m_e c^2)$. We find that in this case, β_{A} need be larger than 0.09, which is translated to $n_{\text{p}} < 2.4 \times 10^{-8} \text{ cm}^{-3}$. A very low baryon density of the jet is needed.

4.3. The jet-orbit misalignment

In our calculations, the jet inclination angle θ_{jet} is set as the same value with i , based on the theoretical framework where relativistic jets are launched along black hole

spin axes (R. D. Blandford & R. L. Znajek 1977), with the spin axis orientation assumed to be perpendicular to the accretion disk plane. Notably, during its 1999 flaring state, V4641 Sgr exhibited a transient radio jet with highly relativistic bulk motions at the small scale, implying that the jet should be nearly aligned with the observer’s line of sight at launch (J. A. Orosz et al. 2001). Subsequent Chandra observations further reveal that broad X-ray emission lines persists over four orders of magnitude in the X-ray luminosity, consistent with Doppler broadening from a high-speed jet viewed at low inclination (E. Gallo et al. 2014). These scenarios introduce a conflict that the inferred low jet inclination angle ($\theta_{\text{jet}} < 10^\circ$) is significantly misaligned with the orbital plane’s normal, posing a puzzling contradiction.

In fact, the jet-orbit misalignment, or spin-orbit misalignment has been found in several binary systems, such as Cygnus X-1 (A. A. Zdziarski et al. 2023) and MAXI J1820+070 (J. Poutanen et al. 2022). Among all of them, V4641 Sgr remains special for its large misalignment angle ($> 50^\circ$). Models such as precessing jets (E. Gallo et al. 2014) and natal kick evolution (G. Salvesen & S. Pokawanvit 2020) have been proposed to explain the spin-orbit misalignment of the source; However, the former remains to be unproven and the latter struggles to account for such a large misalignment angle. Simulations from population synthesis (PS) models also tell that only a minor part of the XRB population ($< 5\%$) could reach $> 20^\circ$ misalignment angles (T. Fragos et al. 2010). So far, the exact origin of the misalignment is still under debate. Nevertheless, considering the mild-relativistic jet with $\Gamma \gtrsim 1$ and weak beaming effects, the actual inclination angle of the jet would not bring significant impacts on our results.

5. CONCLUSIONS

In this paper, we investigated the possibility of interpreting the UHE gamma-ray emission of V4641 Sgr with a leptonic model. We speculated that the elongated UHE morphology of V4641 Sgr arises from electrons accelerated along the jets of the microquasar. Such a kind of ‘distributed’ acceleration may be achieved with the shear acceleration. It has been suggested that jets with velocity-shear flows have the potential to accelerate electrons to $\sim \text{PeV}$ level with this mechanism given favorable parameters. We apply the mechanism to V4641 Sgr. The electron spectrum is obtained by analytically solving the Fokker-Planck equation, with taking into account the pre-acceleration of particles by the stochastic acceleration, cooling and diffusive escape of particles, and high-order resonance scattering between wave and particles. We find that the observed gamma-

ray spectrum can be well reproduced with the IC radiation of accelerated electrons generated by the spectral model. Using the MCMC algorithm, the obtained magnetic field inside the jet under four chose values of R_{jet} are convergently constrained at μG level and the bulk jet speed is around $0.6c - 0.7c$. We also calculated the X-ray synchrotron emission from the same electron population, whose total flux in $2 - 10\text{ keV}$ could range from 10^{-13} to $10^{-12}\text{ erg cm}^{-2}\text{ s}^{-1}$. Recent observations of XRISM (H. Suzuki et al. 2025) on V4641 Sgr may favor $R_{\text{jet}} > 1\text{ pc}$.

Future observations in X-ray band and TeV-PeV gamma-ray band are crucial to test the model. Com-

pared with the hadronic models of escaping protons (Y. Ohira 2024; A. Neronov et al. 2025), our leptonic model provides a relatively strong constraint on the magnetic field of the jet and future X-ray observations of full coverage of the UHE source may give a stronger constraint on the model. Also, our model would predict a truly elongated morphology of the UHE gamma-ray source, whereas the jet-termination scenario or two-lobe scenario (R. Alfaro et al. 2024) would predict two separate sources. The morphology can be hopefully measured at a better precision with future observations of imaging air Cherenkov telescopes such as LACT (S. Zhang et al. 2024), CTA (M. Actis et al. 2011), and ASTRI (S. Scuderi et al. 2022).

APPENDIX

A. THE HIGH-ORDER RESONANCE SCENARIO

In the cosmic-ray transport theories, the spatial diffusion coefficient κ is linked with the pitch-angle coefficient $D_{\mu\mu}$, where μ represents the cosine angle between the particles and the magnetic field lines (U. Jaekel & R. Schlickeiser 1992):

$$\kappa \propto \int_0^1 \frac{(1 - \mu^2)^2}{D_{\mu\mu}} d\mu. \quad (\text{A1})$$

$D_{\mu\mu}$ for the idealized case can be obtained with quasi-linear theory, written as Eq. (A2) (C. Demidem et al. 2020) if the MHD wave is dominated by Alfvén modes:

$$\begin{aligned} D_{\mu\mu}^A &= \frac{\Omega^2 \pi^2 (1 - \mu^2)}{2B_0^2} \sum_{\pm} \sum_{n=-\infty}^{n=\infty} \int \int dk_{\perp} dk_{\parallel} k_{\perp} \\ &\quad \times \delta(k\mu_k\mu - \omega_A + n\Omega) [J_{n+1}(z_{\perp}) + J_{n-1}(z_{\perp})]^2 k_{\parallel}^{-2} \\ &\quad \times (k_{\parallel} - \mu\omega_A)^2 S_k^A, \\ z_{\perp} &= \frac{(k\sqrt{1 - \mu_k^2}) \sqrt{1 - \mu^2}}{\Omega}, \\ \Omega &= \frac{c}{r_L}, \quad \omega_A = \pm\beta_A k_{\parallel}, \quad k_{\parallel} = k\mu_k, \end{aligned} \quad (\text{A2})$$

where k represents the wave number vectors and μ_k is the cosine angle between the wave vectors and the magnetic field lines. k_{\parallel} and k_{\perp} are parallel and vertical components of k with respect to the B_0 direction, respectively. S_k^A is defined as the power spectrum of the turbulence, and the resonance function is in the idealized, undamped form. The longest wavelength Λ_{max} can be transformed to the minimum wave number k_{min} . Noting that $k > k_{\text{min}}$ and the resonance condition requires that $k\mu_k\mu - \omega_A + n\Omega = 0$, we have $|n| > r_L k_{\text{min}}$. It is evident that when $r_L < \Lambda_{\text{max}}$ ($r_L k_{\text{min}} < 1$), the low-order resonant terms will take over, making it easier for particle-wave scatterings to happen. While if $r_L > \Lambda_{\text{max}}$ ($r_L k_{\text{min}} > 1$), only large n values are allowed. As a result, the wave-particle resonance becomes weaker.

After applying the Goldreich-Sridhar power spectrum (see Eq. (12) from C. Demidem et al. (2020)) and summing up all the numerical integrations, we find that $D_{\mu\mu} \propto (r_L k_{\text{min}})^{-2}$, which is coherent with the results obtained in C. Demidem et al. (2020). It indicates that $\kappa \propto r_L^2$ when $r_L > \Lambda_{\text{max}}$. Assuming $r_L(\gamma_{\text{rsn}}) = \Lambda_{\text{max}}$, for more energized electrons ($\gamma > \gamma_{\text{rsn}}$), their MFPs could be rewritten as:

$$\lambda = c\tau_{\text{sc}} = (\xi\Lambda_{\text{max}})^{-1} r_L^2, \quad (\text{A3})$$

causing a higher rate for both SHA and escape, along with an earlier cutoff due to the confinement of MFP.

B. DERIVATION OF THE MODIFIED SPECTRUM

When $r_L > \Lambda_{\max}$, substituting Eq. (A3) into the expressions of the coefficients, Eq. (13), Eq. (14) and Eq. (18) becomes:

$$\begin{aligned} \left\langle \frac{\Delta\gamma^2}{\Delta t} \right\rangle_{\text{SHA}} &= \bar{A}_{\text{SHA}}\gamma^4, \\ \left\langle \frac{\Delta\gamma}{\Delta t} \right\rangle_{\text{SHA}} &= 3\bar{A}_{\text{SHA}}\gamma^3, \\ t_{\text{esc}} &= A_{\text{esc}}\gamma^{-2}. \end{aligned} \quad (\text{B4})$$

According to Figure 3, the cooling timescale becomes much longer than acceleration timescale in this case, thus the cooling term can be neglected. With $\langle \dot{\gamma}_c \rangle = 0$, Eq. (2) turns to the form:

$$\gamma^2 \frac{\partial^2 n}{\partial \gamma^2} + 2\gamma \frac{\partial n}{\partial \gamma} - 2 \left(3 + \frac{2}{A_{\text{esc}} \bar{A}_{\text{SHA}}} \right) n = 0, \quad (\text{B5})$$

which is a typical Cauchy-Euler equation. Substituting the trial solution $n \propto \gamma^r$, we have the relation:

$$\left[r^2 + r - 2 \left(3 + \frac{2}{A_{\text{esc}} \bar{A}_{\text{SHA}}} \right) \right] \gamma^r = 0. \quad (\text{B6})$$

Noting that for the quadratic equation with one variable, $\Delta > 0$ can be guaranteed. So the solutions are:

$$r_{\pm} = -\frac{1}{2} \pm \sqrt{\frac{25}{4} + \frac{2}{A_{\text{esc}} \bar{A}_{\text{SHA}}}}, \quad (\text{B7})$$

thus Eq. (26) can be obtained. It is necessary to point out that here the diffusive approximation is still applied to calculate the escaping rate. However, when the MFPs of the electrons become large enough, it might not be reasonable to describe the escape of particles as diffusion processes because the lacking in efficient wave-particle resonance would make electrons propagate through the jet ballistically. Further studies involving intense MHD simulations are needed to explain the wave-particle interactions and acceleration processes in this situation.

REFERENCES

- Abramowitz, M., & Stegun, I. A. 1948, Handbook of mathematical functions with formulas, graphs, and mathematical tables, Vol. 55 (US Government printing office)
- Actis, M., Agnetta, G., Aharonian, F., et al. 2011, *Experimental Astronomy*, 32, 193, doi: [10.1007/s10686-011-9247-0](https://doi.org/10.1007/s10686-011-9247-0)
- Aharonian, F., Kelner, S., & Prosekin, A. Y. 2010, *Physical Review D—Particles, Fields, Gravitation, and Cosmology*, 82, 043002
- Alfaro, R., Alvarez, C., Arteaga-Velázquez, J., et al. 2024, *Nature*, 634, 557
- Berezhko, E., & Krymskii, G. 1981, *Sov. Astron. Lett.(Engl. Transl.):(United States)*, 7
- Blandford, R. D., & Znajek, R. L. 1977, *Monthly Notices of the Royal Astronomical Society*, 179, 433
- Bosch-Ramon, V., & Khangulyan, D. 2009, *International Journal of Modern Physics D*, 18, 347
- Coppi, P. S., & Aharonian, F. A. 1997, *ApJL*, 487, L9, doi: [10.1086/310883](https://doi.org/10.1086/310883)
- Demidem, C., Lemoine, M., & Casse, F. 2020, *Physical Review D*, 102, 023003
- Dermer, C. D., & Menon, G. 2009,
- Earl, J., Jokipii, J., & Morfill, G. 1988, *Astrophysical Journal, Part 2-Letters (ISSN 0004-637X)*, vol. 331, Aug. 15, 1988, p. L91-L94., 331, L91
- Fragos, T., Tremmel, M., Rantsiou, E., & Belczynski, K. 2010, *The Astrophysical Journal Letters*, 719, L79
- Gabuzda, D. C. 2014, in *The Formation and Disruption of Black Hole Jets (Springer)*, 117–148
- Gallo, E., Plotkin, R. M., & Jonker, P. G. 2014, *Monthly Notices of the Royal Astronomical Society: Letters*, 438, L41
- Gandhi, P., Rao, A., Johnson, M. A., Paice, J. A., & Maccarone, T. J. 2019, *Monthly Notices of the Royal Astronomical Society*, 485, 2642

- H. E. S. S. Collaboration, Abdalla, H., Adam, R., et al. 2020, *Nature*, 582, 356, doi: [10.1038/s41586-020-2354-1](https://doi.org/10.1038/s41586-020-2354-1)
- He, J.-C., Sun, X.-N., Wang, J.-S., et al. 2023, *MNRAS*, 525, 5298, doi: [10.1093/mnras/stad2542](https://doi.org/10.1093/mnras/stad2542)
- Hillas, A. M. 1984, IN: Annual review of astronomy and astrophysics. Volume 22. Palo Alto, CA, Annual Reviews, Inc., 1984, p. 425-444., 22, 425
- Jaekel, U., & Schlickeiser, R. 1992, *Journal of Physics G: Nuclear and Particle Physics*, 18, 1089
- Jokipii, J., & Morfill, G. 1990, *Astrophysical Journal*, Part 1 (ISSN 0004-637X), vol. 356, June 10, 1990, p. 255-258., 356, 255
- Khangulyan, D., Aharonian, F. A., & Kelner, S. R. 2014, *The Astrophysical Journal*, 783, 100
- Kulsrud, R. M. 2020, *Plasma physics for astrophysics* (Princeton University Press)
- Laing, R., & Bridle, A. 2014, *Monthly Notices of the Royal Astronomical Society*, 437, 3405
- LHAASO Collaboration. 2024, arXiv e-prints, arXiv:2410.08988, doi: [10.48550/arXiv.2410.08988](https://doi.org/10.48550/arXiv.2410.08988)
- Liu, R.-Y., Rieger, F. M., & Aharonian, F. A. 2017, *The Astrophysical Journal*, 842, 39
- Liu, R.-Y., & Wang, X.-Y. 2021, *ApJ*, 922, 221, doi: [10.3847/1538-4357/ac2ba0](https://doi.org/10.3847/1538-4357/ac2ba0)
- MacDonald, R. K., Bailyn, C. D., Buxton, M., et al. 2014, *The Astrophysical Journal*, 784, 2
- Mertsch, P. 2011, *Journal of Cosmology and Astroparticle Physics*, 2011, 010
- Nagai, H., Haga, T., Giovannini, G., et al. 2014, *The Astrophysical Journal*, 785, 53
- Neronov, A., Oikonomou, F., & Semikoz, D. 2025, *Physical Review D*, 111, 103025
- Ohira, Y. 2024, arXiv preprint arXiv:2410.22976
- Orosz, J. A., Kuulkers, E., van der Klis, M., et al. 2001, *The Astrophysical Journal*, 555, 489
- Poutanen, J., Veledina, A., Berdyugin, A. V., et al. 2022, *Science*, 375, 874
- Revnivtsev, M., Gilfanov, M., Churazov, E., & Sunyaev, R. 2002, *Astronomy & Astrophysics*, 391, 1013
- Rieger, F. M. 2019, *Galaxies*, 7, 78
- Rieger, F. M., Bosch-Ramon, V., & Duffy, P. 2007, in *The Multi-Messenger Approach to High-Energy Gamma-Ray Sources*, Springer, 119–125
- Rieger, F. M., & Duffy, P. 2006, *The Astrophysical Journal*, 652, 1044
- Rieger, F. M., & Duffy, P. 2019, *The Astrophysical Journal Letters*, 886, L26
- Salvesen, G., & Pokawanvit, S. 2020, *Monthly Notices of the Royal Astronomical Society*, 495, 2179
- Schlickeiser, R., Vainio, R., Böttcher, M., et al. 2002, *Astronomy & Astrophysics*, 393, 69
- Scuderi, S., Giuliani, A., Pareschi, G., et al. 2022, *Journal of High Energy Astrophysics*, 35, 52, doi: [10.1016/j.jheap.2022.05.001](https://doi.org/10.1016/j.jheap.2022.05.001)
- Suzuki, H., Tsuji, N., Kanemaru, Y., et al. 2025, *The Astrophysical Journal Letters*, 978, L20
- Wang, J.-S., Reville, B., Liu, R.-Y., Rieger, F. M., & Aharonian, F. A. 2021, *Monthly Notices of the Royal Astronomical Society*, 505, 1334
- Wang, J.-S., Reville, B., Mizuno, Y., Rieger, F. M., & Aharonian, F. A. 2023, *MNRAS*, 519, 1872, doi: [10.1093/mnras/stac3616](https://doi.org/10.1093/mnras/stac3616)
- Wang, J.-S., Reville, B., Rieger, F. M., & Aharonian, F. A. 2024, *ApJL*, 977, L20, doi: [10.3847/2041-8213/ad9589](https://doi.org/10.3847/2041-8213/ad9589)
- Webb, G., Barghouty, A., Hu, Q., & Le Roux, J. 2018, *The Astrophysical Journal*, 855, 31
- Webb, G. M., Al-Nussirat, S., Mostafavi, P., et al. 2019, *ApJ*, 881, 123, doi: [10.3847/1538-4357/ab2fca](https://doi.org/10.3847/1538-4357/ab2fca)
- Zabalza, V. 2015, arXiv preprint arXiv:1509.03319
- Zdziarski, A. A., Veledina, A., Szanecki, M., et al. 2023, *The Astrophysical Journal Letters*, 951, L45
- Zhang, S., Wang, Y., Liu, J., et al. 2024, in 38th International Cosmic Ray Conference, 808
- Zhao, Z., Li, J., & Torres, D. F. 2025, arXiv preprint arXiv:2503.16844

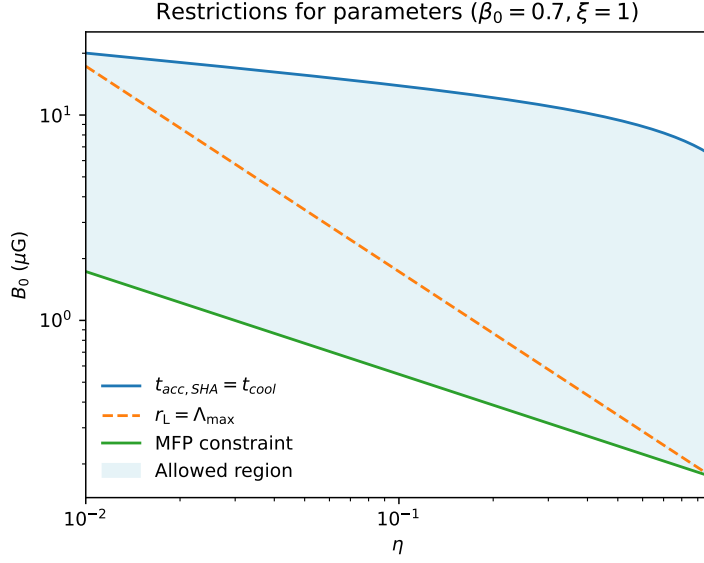


Figure 1. $\eta - B_0$ planes which show the potential parameter sets under two confinements: $c\tau_{\text{sc}} \leq R_{\text{jet}}$ and $t_{\text{acc,SHA}} \leq t_c$, with $\beta_0 = 0.7$, $q=5/3$, $R_{\text{jet}} = 5$ pc and $\gamma = 0.8$ PeV / $(m_e c^2)$. The orange dashed line indicates the limit for the 1st-order resonance and the shaded area represents the allowed parameter regions when $\xi = 1$.

Table 1. Best-fit parameters from χ^2 tests

Parameters	Jet radius R_{jet}			
	5 pc	3 pc	1 pc	0.5 pc
$\log B_0$ (μG)	$-0.32^{+0.20}_{-0.35}$	$-0.02^{+0.13}_{-0.40}$	$0.49^{+0.07}_{-0.45}$	$0.73^{+0.10}_{-0.40}$
η ($R_{\text{shear}}/R_{\text{jet}}$)	$0.38^{+0.39}_{-0.13}$	$0.29^{+0.43}_{-0.07}$	$0.28^{+0.46}_{-0.05}$	$0.30^{+0.44}_{-0.06}$
β_0 (Spine velocity)	$0.70^{+0.21}_{-0.08}$	$0.64^{+0.25}_{-0.05}$	$0.62^{+0.28}_{-0.02}$	$0.65^{+0.25}_{-0.03}$
$\log N_{\text{tot}}$ (Norm.)	$46.90^{+0.72}_{-1.02}$	$46.42^{+1.47}_{-0.43}$	$46.59^{+1.95}_{-0.49}$	$46.42^{+2.17}_{-0.25}$
$\chi^2/\text{d.o.f.}$	13.5/12	13.5/12	13.4/12	13.5/12

Notes: Parameters derived from χ^2 minimization across different jet radius scales.

Table 2. Best-fit parameters from χ^2 tests, with $R_{\text{jet}} = 3$ pc

Parameters	Type of turbulence	
	$q = 3/2$	$q = 2$
$\log B_0$ (μG)	$-0.09^{+0.10}_{-0.36}$	$0.16^{+0.14}_{-0.49}$
η ($R_{\text{shear}}/R_{\text{jet}}$)	$0.42^{+0.31}_{-0.20}$	$0.11^{+0.21}_{-0.01}$
β_0 (Spine velocity)	$0.78^{+0.15}_{-0.10}$	$0.38^{+0.25}_{-0.01}$
$\log N_{\text{tot}}$ (Norm.)	$46.51^{+0.84}_{-0.76}$	$51.67^{+0.50}_{-1.41}$
$\chi^2/\text{d.o.f.}$	13.6/12	13.4/12

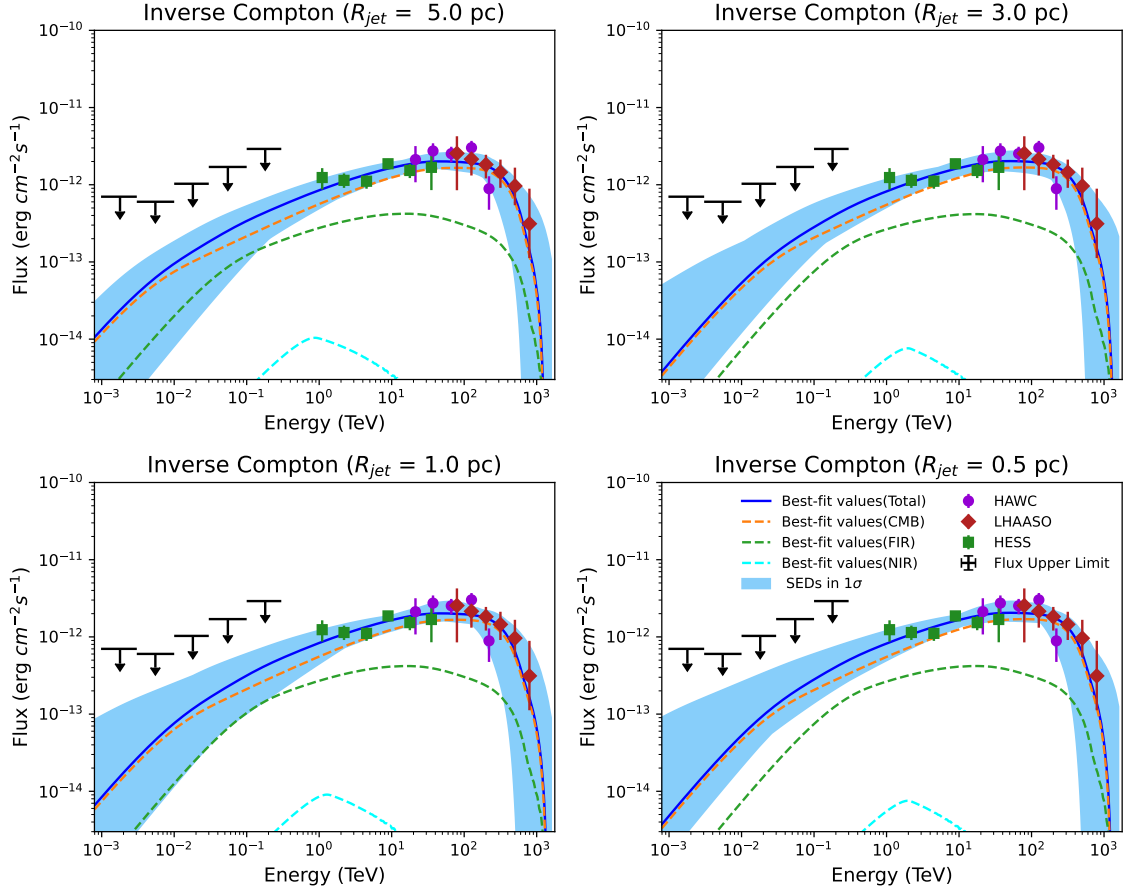


Figure 2. The fitting results for the UHE spectrum of V4641 Sgr, with data points from HAWC (R. Alfaro et al. 2024), LHAASO (LHAASO Collaboration 2024) and H.E.S.S. (A. Neronov et al. 2025). The upper limits in 1 - 300 GeV are extracted from Z. Zhao et al. (2025). The blue solid lines indicate the spectral energy distributions (SEDs) of total IC emission from three photon fields and the lightblue regions are composed of possible fitting results in 1σ range of further χ^2 tests.

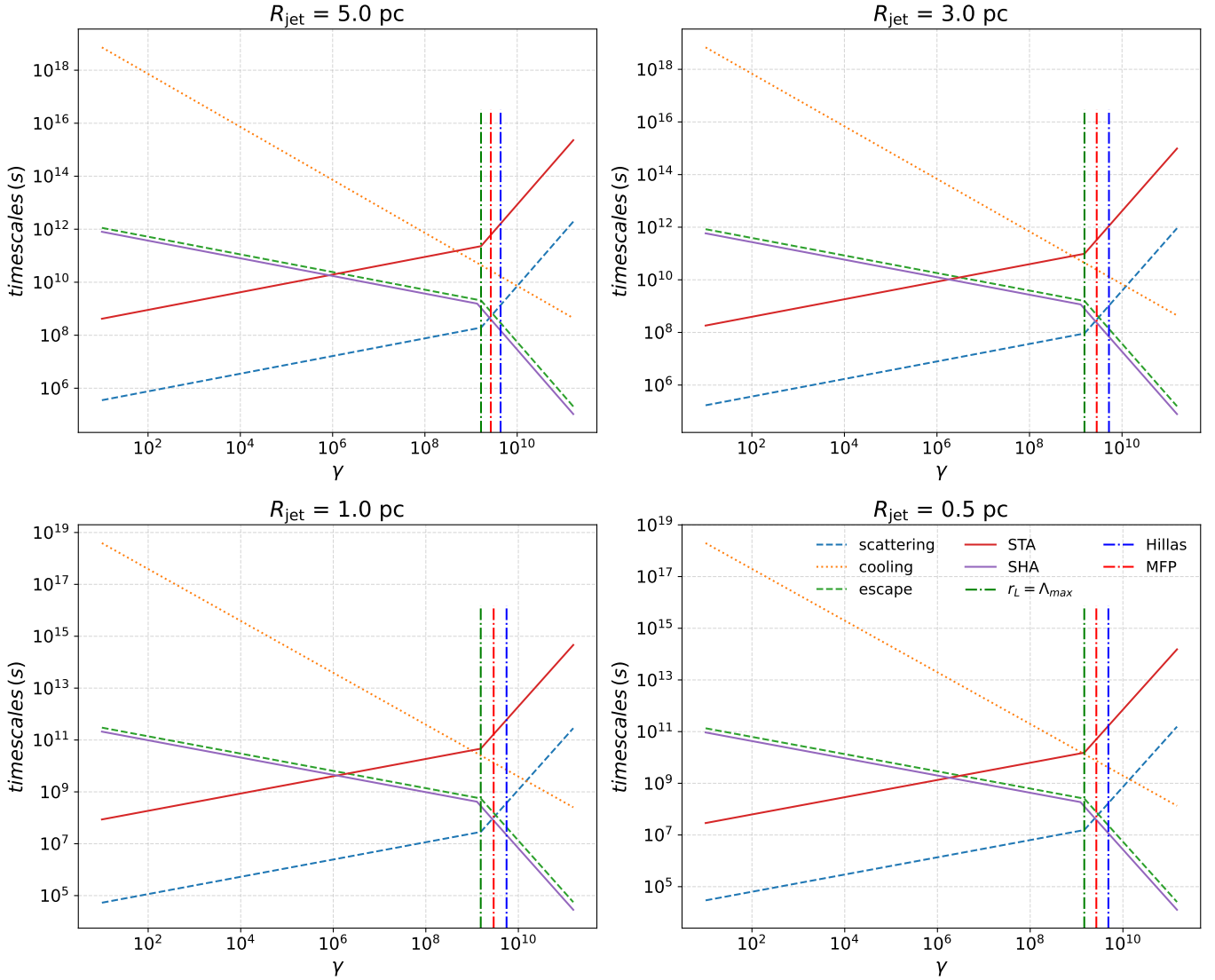


Figure 3. Timescales for different processes with the best-fit parameters in 3.1, derived from equation (4), (8), (14), (17) and (18). The red solid line represents the timescale for stochastic acceleration (STA) and the purple one represents the one for shear acceleration (SHA); The orange dotted line shows the timescale for radiative cooling and the blue dashed line is the scattering timescale for electrons in the jet; The dash-dotted lines indicate the extra limitations caused by the Hillas criterion (γ_{Hillas}) and the particle mean free path (MFP) (γ_{MFP}).

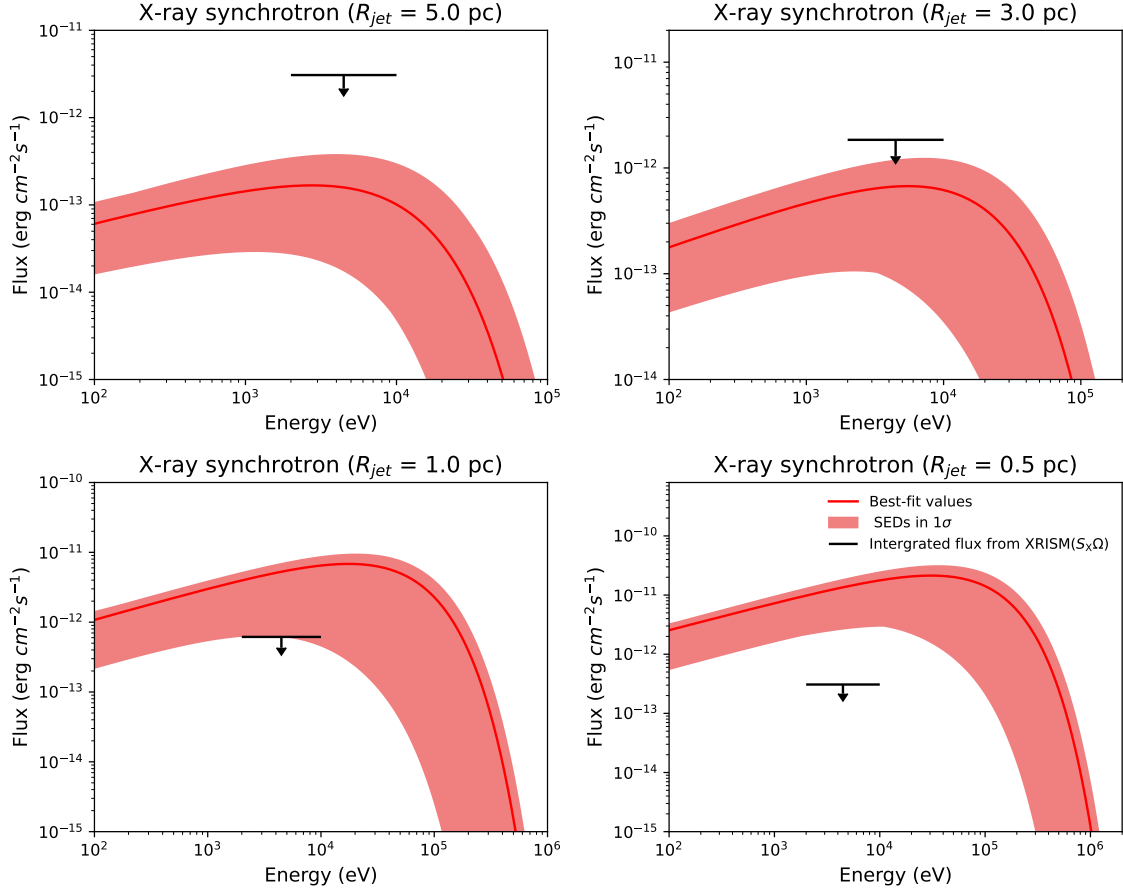


Figure 4. The synchrotron emission produced by the same electron population responsible for the UHE gamma-ray emission. The red solid lines represent the emission under the best-fit parameters and the reddish regions are composed of predicted emission with possible spectral energy distributions (SEDs) in 1σ range of χ^2 tests, which is coherent with the ones shown in Figure 2. The black solid lines represent the total integrated flux inferred from the surface brightness obtained by XRISM (H. Suzuki et al. 2025) from 2 to 10 keV.

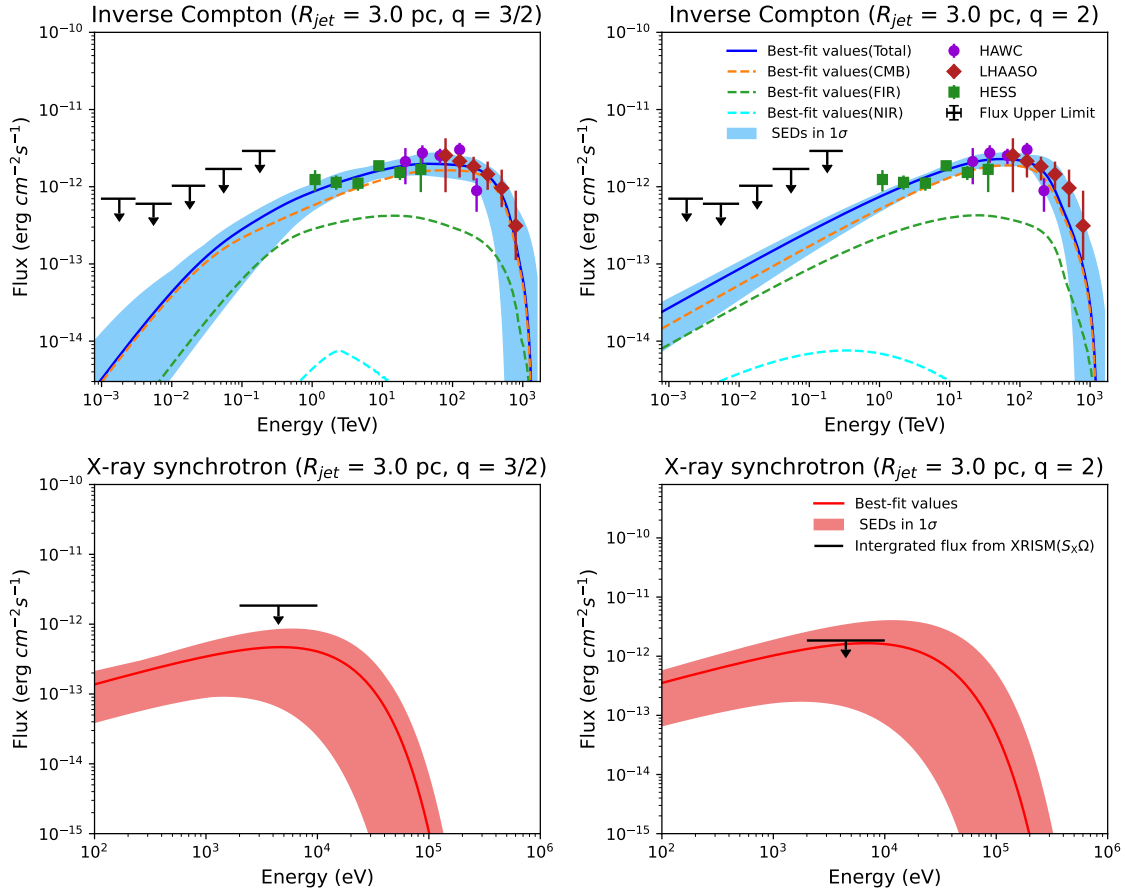


Figure 5. The fitting results for the UHE spectrum and predicted X-ray synchrotron flux, with different types of turbulence. The left-side panels show results from the Kraichnan-type ($q = 3/2$) while the right-side panels show that from the hard-sphere limit ($q = 2$). Both of the two cases can explain the observations, with only minor impacts on crucial parameters.